Surface & Coatings Technology 304 (2016) 98–107

Contents lists available at ScienceDirect

Surface & Coatings Technology

journal homepage: www.elsevier.com/locate/surfcoat

# Cubic $\beta$-$WN_x$ layers: Growth and properties vs N-to-W ratio

B.D. Ozsdolay [a], C.P. Mulligan [b], K. Balasubramanian [a], Liping Huang [a], S.V. Khare [c], D. Gall [a,*]

[a] Department of Materials Science and Engineering, Rensselaer Polytechnic Institute, Troy, NY 12180, USA
[b] U.S. Army Armament Research Development & Engineering Center, Benet Laboratories, Watervliet, NY 12189, USA
[c] Department of Physics and Astronomy, University of Toledo, 2801 West Bancroft Street, Toledo, OH 43606, USA

ARTICLE INFO

*Article history:*
Received 18 March 2016
Revised 27 June 2016
Accepted in revised form 28 June 2016
Available online 29 June 2016

*Keywords:*
Tungsten nitride
Cubic
Nitrogen vacancy
Hardness
Density functional calculations
Lattice constant

ABSTRACT

Tungsten nitride layers, 1.45-μm-thick, were deposited by reactive magnetron sputtering on MgO(001), MgO(111), and $Al_2O_3$(0001) in 20 mTorr $N_2$ at $T_s$ = 500–800 °C. All layers deposited at $T_s$ = 500–700 °C form a cubic phase, as determined by X-ray diffraction $\omega$-$2\theta$ scans, and show an N-to-W ratio $x$ that decreases from $x$ = 1.21 to 0.83 with increasing $T_s$ = 500–700 °C, as measured by energy dispersive and photoelectron spectroscopies. $T_s$ = 500 and 600 °C yields polycrystalline predominantly 111 oriented $\beta$-WN on all substrates. In contrast, deposition at 700 °C results in epitaxial growth of $\beta$-WN(111) and $\beta$-WN(001) on MgO(111) and MgO(001), respectively, and a 111-preferred orientation on $Al_2O_3$(0001). $T_s$ = 800 °C causes nitrogen loss and $WN_x$ layers with primarily BCC W grains and $x$ = 0.04–0.06. Density functional theory calculations indicate an increase in structural stability by the introduction of either W or N vacancies into the cubic rock-salt structure, reducing the formation energy per atom from 0.32 eV for the rock-salt structure to 0.09 eV for $WN_{0.75}$ and −0.07 eV for $WN_{1.33}$, and to −0.42 eV for stoichiometric WN in the NbO structure. The out-of-plane lattice constant decreases from 4.357–4.169 Å with increasing $T_s$ = 500–700 °C. Comparing these values with calculated lattice constants indicates that the W vacancy concentration increases from 6–11% for $T_s$ = 500–600 °C to 11–18% for $T_s$ = 700 °C, while the N vacancy concentration also increases from negligible to 18–29%. The simultaneous increase of both vacancy types is attributed to thermally activated $N_2$ recombination and desorption and atomic rearrangement towards the thermodynamically favorable cubic NbO structure which contains 25% of both W and N vacancies. The measured elastic modulus ranges from 110 to 260 GPa for 500–700 °C and decreases with increasing N-content, and increases to 350 GPa for $T_s$ = 800 °C. The room temperature resistivity decreases with increasing $T_s$ = 500–700 °C from 4.5–1.1 × $10^3$ μΩ-cm, indicating a resistivity decrease with decreasing nitrogen content and increasing crystalline quality and phase purity.



## 1. Introduction

Transition metal nitrides are known for their high hardness, wear and corrosion resistance, and high temperature stability [1–3], and are therefore widely used as hard wear-protective coatings, diffusion barriers in microelectronics, and optical or decorative coatings [4,5]. Many computational and experimental studies focus on the analysis of stoichiometric samples [6–10]. However, the properties of transition metal nitrides can vary widely as a function of the anion to cation ratio $x$. For example, the hardness of $TiN_x$ decreases from 30 ± 2 to 20.2 ± 2 GPa and its electrical resistivity decreases from 192 to 13 μΩ-cm as $x$ increases from 0.67 to 1.00 while retaining the single cubic phase [11,12]. In addition, many transition metal nitrides including $HfN_x$ [13], $TiN_x$ [11], $CeN_x$ [14], $ZrN_x$, [15], $TaN_x$ [16] and $NbN_x$ [17] crystallize in a range of different phases, resulting in additional variations in physical properties. That is, the nitrogen-to-metal ratio affects both the crystal structure, i.e. the phase, and the composition of this phase as manifested by point defects including metal and/or nitrogen vacancies and anti-site substitutions [18]. The understanding of how the crystal structure and the point defect concentration of transition metal nitride layers changes with composition and deposition conditions is important in order to develop protective coatings with desired properties, since these properties are affected by both the crystal structure and the defect concentration.

Tungsten nitride exhibits a variety of phases over a large composition range $x$ = 0.5–2.0 [19–22]. The most commonly reported $WN_x$ phases are stoichiometric hexagonal δ-WN and cubic $\beta$-$W_2N$, which is a rocksalt-type structure where 50% of the N-sites are vacant [19,20]. In addition, there are reports on hexagonal and rhombohedral $W_2N_3$ and cubic $W_3N_4$ phases which have been synthesized using high pressure and high temperature [22]. Reports from first-principles computational studies propose a high-bulk-modulus $WN_2$ phase [21], a cubic NbO structure for stoichiometric WN [23–25], a tungsten-deficient rhombohedral r-$W_2N_3$ [25], as well as metastable phases including, for example, a hexagonal δ-$W_2N_3$ structure [25]. Interestingly, these studies found no stable cubic β-$W_2N$ structure and the cubic rock-salt-based $\beta$-WN structures are only stable when containing W vacancies [25].

* Corresponding author.
*E-mail address:* galld@rpi.edu (D. Gall).

http://dx.doi.org/10.1016/j.surfcoat.2016.06.079
0257-8972/

Nevertheless, experimental studies typically interpret that cubic $\beta$-$WN_x$ exhibits a rock-salt structure [JCPDF 00-025-1257], as X-ray diffraction data matches fcc-structure reflections with, however, a lattice parameter that varies from 4.11–4.30 Å [26–30] and a reported outlier of 3.9 Å possibly due to a low nitrogen concentration [30]. The predicted stable phase for stoichiometric ($x = 1$) $WN_x$ is the cubic NbO structure [23,25], which can be described as a rock-salt structure containing a regular array of 25% cation and 25% anion vacancies [31]. We envision that deviations from stoichiometric compositions may be the result of these vacancies being filled. More specifically, cubic $\beta$-$WN_x$ structures with understoichiometric compositions $0.75 \le x < 1$ may form by anion vacancies of NbO-structure WN being filled by W atoms, and correspondingly, $\beta$-$WN_x$ with $x = 1$–1.33 is obtained by filling cation vacancies with N atoms.

The composition of tungsten nitride layers is affected by deposition parameters and method, which include reactive DC magnetron sputtering [26–28,30,32–37], reactive pulsed laser deposition [34,38,39], RF sputtering [40–42], cathodic arc deposition [43], atomic layer deposition [44], and chemical vapor deposition [29,45–47]. DC reactive magnetron sputtering in a $Ar + N_2$ mixture has been reported to yield $x = 0.33$ with a $N_2$ fraction in the gas of $f_{N2} = 10\%$ [30], or $x = 0$–0.5 with $f_{N2}$ increasing from 0 to 75% [36], but also $x = 0$–1.1 for $f_{N2} = 0$–75% [32], $x = 0$–1.2 for $f_{N2} = 0$–63% [28], and $x = \sim 0$–1.2 for $f_{N2} = 5\%$ with an increasing 17–26 Pa total pressure [37]. However, the layers with high N content $x > 0.9$ have a tendency to exhibit a hexagonal WN phase [28,40]. RF sputter deposition yields in many cases even higher nitrogen concentrations (again exhibiting a hexagonal phase for high $x$), likely due to energetic implantation, with $x = 0.6$–1.6 for $f_{N2} = 10$–75% [41], $x = 1.1$–1.4 for $f_{N2} = 10$–60% [42], $x = 0.11$–0.25 for $P_{N2} = 0$–1.6 Pa with a constant 0.53 Pa Ar [34], and $x = 0.35$–1.17 for $f_{N2} = 38$–83% [40]. Pulsed laser deposition (PLD) can also lead to a wide range of nitrogen contents including $x = 0.17$–0.5 in 1.33–8 Pa $N_2$ [34] and a high nitrogen content of $x = 1.76$ in 75 mTorr $N_2$ [39]. In comparison to these previously reported concentration ranges for cubic $\beta$-$WN_x$, our layers have a relatively high nitrogen concentration.

In this study, we report on polycrystalline and epitaxial $WN_x$ layers deposited on single crystal MgO(001), MgO(111), and $Al_2O_3$(0001) substrates. The layers deposited from $T_s = 500$–700 °C have relatively large N/W ratios ranging from $x = 0.83$–1.21 and exhibit a pure cubic $\beta$-phase, indicating that the composition range for $\beta$-$WN_x$ can be extended from well below to well above the stoichiometric $x = 1$, which is opposite to the reported formation of a hexagonal phase for $WN_x$ with $x > 0.9$ [28,40]. The nitrogen content $x$ decreases with increasing growth temperature and nearly vanishes for $T_s = 800$ °C, yielding $WN_x$ layers with a predominantly BCC W structure. Density functional theory (DFT) calculations provide a confirmation of lattice constant trends observed with decreasing nitrogen content. In addition, DFT computations are also used to examine the relative stabilities of rock-salt and NbO structures of $WN_x$ as a function of $x$. They indicate a negative formation energy for the formation of both W and N vacancies and provide a framework to explain the increasing vacancy concentrations on both cation and anion sublattices with increasing $T_s$. Nanoindentation results show similar hardness trends for all three substrates ranging from 9.7–12.9 GPa for $WN_x$ deposited from 500 to 700 °C, within the reported hardness $H$ values for $WN_x$ of 5–39 GPa [28,33,34,38,40,43], while the elastic moduli vary considerably with N-content and texture, ranging from 110 to 260 GPa, which is lower than previously reported values of $E = 240$–430 GPa [32,34,40]. In addition, four point probe measurements show a decrease in resistivity with increasing substrate temperature due to a combination of increasing crystal quality and decreasing nitrogen content.

## 2. Experimental procedure

$WN_x$ layers were deposited on MgO(001), MgO(111) and $Al_2O_3$(0001) substrates in a load-locked ultra-high vacuum (UHV) dc magnetron sputtering system with a base pressure of $<10^{-9}$ Torr [17,48]. The substrates are one-side polished $10 \times 10 \times 0.5$ $mm^3$ wafers that were cleaned in successive rinses of trichloroethylene, acetone, isopropanol, and deionized water, blown dry with dry $N_2$, attached to a Mo block with silver paint, loaded into the system through a load-lock chamber, and thermally degassed at 900 °C for 1 h. The substrate temperature $T_s$ was measured by a thermocouple below the sample stage that was cross-calibrated with a pyrometer focusing on the sample surface. $T_s$ was lowered to 500–800 °C prior to deposition from a 99.95%-pure 51-mm-diameter W target which was sputter etched for 5 min with a shutter shielding the substrate. The target was facing the substrate at a 9 cm distance and from a 45° angle, with the substrate being continuously rotated at 60 $min^{-1}$ to increase thickness uniformity. A constant dc power of 300 W was applied to the magnetron, yielding a deposition rate of 375 nm/h in 20 mTorr 99.999% pure $N_2$.

X-ray diffraction was done in a Panalytical X'Pert PRO MPD system with a Cu $K_\alpha$ $\lambda = 1.5418$ Å source yielding a 1° divergent incident beam limited by an incident slit. $\omega$-$2\theta$ scans were collected over a $2\theta$ range from 5°–90° using the Bragg-Brentano geometry and a PixCEL solid-state line detector. The $2\theta$-values were calibrated using the substrate peaks, that is, $2\theta$ was set to the literature values of 36.947°, 42.909°, and 41.685° at the measured positions of the MgO 111, MgO 002, and $Al_2O_3$ 0006 reflections measured using Cu $K\alpha_1$ X-rays, respectively. Energy-dispersive X-ray spectroscopy (EDS) spectra were collected in a FEI Helios Nanolab scanning electron microscope (SEM) with an accelerating voltage of 5.0 kV and a working distance of 5.0 mm. The EDS spectra were analyzed with the Oxford Instruments AZtec EDS software to determine the N-to-W composition ratio of each sample. The composition values are expected to be accurate to within ±3%, based on test measurements on BN and $CaSiO_3$ standards that use the same Oxford Instruments X-Max$^N$ 80 silicon drift detector used for the $WN_x$ specimens and is particularly well suited for light element analysis. In addition, photoelectron spectroscopy (XPS) spectra were acquired for samples deposited at $T_s = 700$ °C using Al $K_\alpha$ radiation (1486.7 eV) in a PHI Versaprobe system with a hemispherical analyzer and an 8-channel detector. All high resolution spectra were collected using a pass energy of 23.5 eV and a step size of 0.2 eV. The XPS analyses were done on as-deposited air exposed surfaces without sputter cleaning in order to not affect the measured N-to-W ratios by preferential sputtering effects.

The hardness and elastic modulus were measured using a Hysitron TI 900 Tribodenter nanoindenter which was calibrated using a fused quartz standard of known hardness and elastic modulus. A minimum of 10 indents were performed for each sample, using a diamond Berkovich tip with a nominal tip radius of 150 nm that was indented to a maximum load of 6 mN. $H$ and $E$ values of the layers were determined from the loading and unloading curves, using the Oliver and Pharr method [49] and an elastic modulus of 1140 GPa and a Poisson's ratio of 0.07 for the diamond indenter tip [50]. Resistivity measurements were done at room temperature (293 K) using a linear four point probe with 1-mm inter-probe spacings, a Keithley 2182A Nanovoltmeter, and a Keithley 6220 Precision Current Source providing ±3 mA. The resistivity was determined from the measured sheet resistance by correcting for the substrate geometry according to Ref. [51], and using the layer thickness of 1.45 μm as measured by cross sectional SEM on cleaved samples.

## 3. Computational method and results

First-principles DFT calculations are performed using the Vienna ab initio simulation package (VASP), employing periodic boundary conditions, a plane wave basis set, the Perdew-Burke-Ernzerhof generalized gradient approximation exchange correlation functional [52], and the projector-augmented wave method [53]. All computational parameters are chosen such that calculated total energy differences are converged to within 5 meV/atom. This includes a 500 eV cut-off energy for the

plane-wave basis set expansion and a Γ-centered 6 × 6 × 6 *k*-point grid for $WN_x$ super cells containing 48–64 atoms. W 4*s*, 4*p*, and 4*d* electrons are explicitly calculated, that is, they are not included in the core of the pseudo potential. Atomic positions and lattice parameters are relaxed iteratively while the cubic unit cell shape was kept fixed for all calculations. The simulated cubic supercells consist of 8 conventional unit cells which each contain 4W and 4N atomic sites, yielding a total of 64 atoms in the super cell for the rock-salt (NaCl) structure. The conventional unit cell of WN in the NbO structure belongs to the space group 221 (*Pm*-3m) with Wyckoff positions W 3c (0, 1/2, 1/2) and N 3d (0 , 1/2, 0), yielding a regular sublattice of 8W and 8N vacancies for the NbO structure supercell containing a total of 48 atoms. Off-stoichiometric cubic $WN_x$ is simulated by varying the occupation on this sublattice. That is, starting with the NaCl structure, an increasing number of W or N sublattice sites are vacated, causing an increase or decrease in *x*, respectively. Correspondingly, starting from the NbO structure, W or N sublattice sites are filled with the respective atoms, causing a decrease or increase in *x*, respectively. For each fixed number of W and N atoms, all possible occupation configurations on the sublattice have been calculated, and the results from the lowest energy configuration are reported in this paper. We note here that other vacancy configurations, i.e. with vacancies occupying other sites than those defined by the regular sublattice of the NbO structure, are not investigated in this study. Also, the generalized gradient approximation used in the calculations is known to typically overestimate lattice constants by approximately 1% [54], which is not corrected for in the below analysis, since there is no systematic method to correct for such lattice-constant errors except by using an alternative exchange correlation functional such as the PBEsol.

The cohesive energy $E_c$ for the different structures is determined relative to BCC W and molecular nitrogen. That is, $E_c = E - N_W\mu_W - 1/2\, N_N\mu_{N2}$, where *E* is the calculated energy for a specific supercell containing $N_W$ tungsten and $N_N$ nitrogen atoms, while $\mu_W$ and $\mu_{N2}$ are the W and $N_2$ chemical potentials corresponding to the calculated energy of a one-atom BCC W unit cell and an isolated $N_2$ molecule, respectively. All calculations are for zero temperature. Considering finite temperatures would add correction terms, with the largest being associated with the entropy of the $N_2$ gas, driving the system at high temperature towards phase separation into $N_2$ gas and a reduction in *x* in the solid $WN_x$ phase. In order to directly compare formation energies $E_f$ of different configurations, the calculated cohesive energies are presented in this paper as energy per atom, i.e. $E_f = E_c / (N_W + N_N)$.

Fig. 1 summarizes the computational results, showing the calculated formation energy and lattice constant of cubic $WN_x$ vs N-to-W ratio $x = 0.75–1.33$. The starting point for all explored atomic configurations are the NaCl and NbO crystal structures, which have calculated formation energies of $E_f = 0.32$ and $-0.42$ eV, as shown in Fig. 1(a) at $x = 1.0$. The positive $E_f$ value for the rock-salt structure indicates that it is unstable against phase separation into BCC W and $N_2$ gas. In contrast, the NbO structure is stable, consistent with previous computational reports [23, 25]. Off-stoichiometric configurations are simulated by creating or filling vacancies in the NaCl or NbO structures, respectively. The formation energy of $WN_x$ in the rock-salt structure drops when introducing W vacancies [plotted as red circles in Fig. 1(a)], initially steeply from 0.32 to 0.04 eV for $x = 1.00–1.14$ and then gently to $-0.07$ eV for $x = 1.33$. Similarly, N-vacancies also reduce $E_f$, reaching 0.11 eV for $x = 0.88$ and 0.09 eV for $x = 0.75$. Filling vacancies of the NbO structure results in an increase in the formation energy, as shown with the blue squares in Fig. 1(a). The increase is initially small, particularly for $x > 1$, but then reaches the same endpoints as the red data points for $x = 0.75$ and 1.33, which correspond to structures with conventional unit cells containing one N and one W vacancy, respectively. In addition, Fig. 1(a) also shows as triangular data point the formation energy for a stoichiometric WN structure with a 50% filling of both cation and anion vacancies in the NbO structure. The $E_f = -0.23$ eV of this structure is considerably closer to the NbO structure than the rock-salt formation energy, confirming

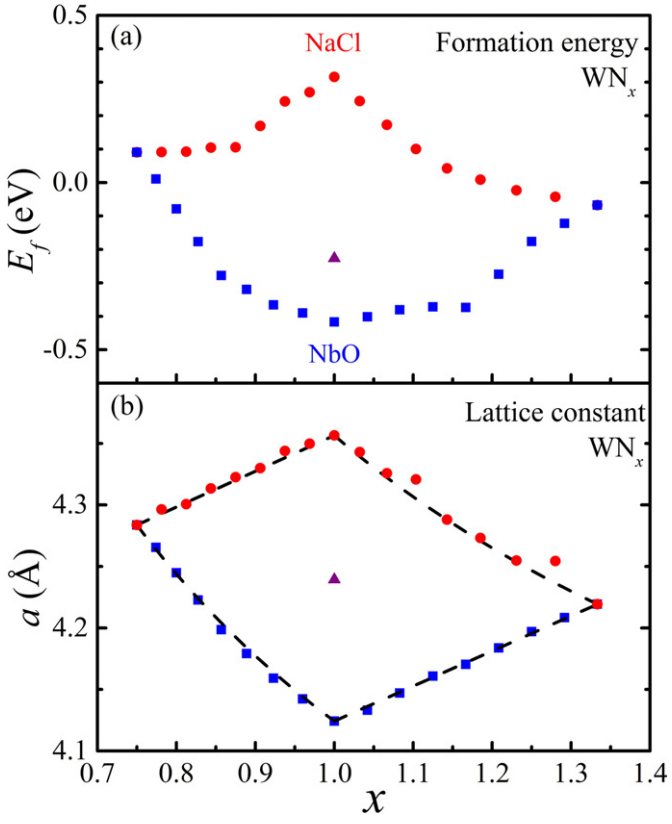


**Fig. 1.** (a) Formation energy per atom $E_f$ and (b) lattice constant *a*, of cubic $WN_x$ as a function of N-to-W ratio *x* obtained from first-principles simulations using a cubic supercell with 32 cation and 32 anion sites. The left top quadrant (red circles, $x < 1$) is for structures with 32W and 24–32N atoms, corresponding to rock-salt $WN_x$ containing N vacancies. Similarly: *right top*: (red circles, $x > 1$), 24–32 W and 32 N atoms; *left bottom*: (blue squares, $x < 1$); 24–32 W and 24 N atoms, *right bottom*: (blue squares, $x > 1$), 24 W and 24–32 N atoms. The triangle is for an ordered structure (28 W and 28 N atoms) half-way between rock-salt and NbO. Dashed lines are obtained from data fitting using Eq. (1). (For interpretation of the references to color in this figure legend, the reader is referred to the web version of this article.)

the observed trend that the introduction of a small density of vacancies in the NaCl structure reduces $E_f$ considerably more than the increase in $E_f$ when filling some vacancy sites in the NbO structure.

Fig. 1(b) is a corresponding plot of the calculated lattice constants. It is $a_{rs} = 4.357$ Å for the NaCl structure, and 5.3% smaller, $a_{NbO} = 4.124$ Å, for the NbO structure. As expected, introducing vacancies in rock-salt WN reduces *a* while filling vacant sites in the NbO structure increases *a*. This results in approximately linear changes in *a* as a function of *x*, as illustrated by the nearly straight dashed lines through the data points in Fig. 1(b). They are obtained using a polynomial expression for the lattice constant as a function of the W and N vacancy concentrations $V_W$ and $V_N$:

$$a = a_{rs} - \alpha V_W - \beta V_N - \gamma V_W V_N, \quad (1)$$

where the parameters $\alpha = 0.549$ Å, $\beta = 0.291$ Å and $\gamma = 0.357$ Å are determined to match the calculated lattice constants for $x = 0.75$, 1.0, and 1.33. Here $V_W$ and $V_N$ are in units of "sites" i.e. they correspond to the probability for a cation or anion site in the rock-salt structure to be vacant. A first test to check the validity of this expression is to calculate the lattice constant for the WN structure with 50% filling, i.e. $V_W = V_N = 0.125$, yielding a lattice constant of 4.246 Å, which is just 0.16% larger than the directly calculated value for this structure of 4.239 Å. This confirms the validity of the expression but also suggests that this structure with perfectly ordered vacancies may be slightly denser than predicted from a more random distribution of vacancies on the

sublattice. The expression in Eq. (1) and the associated parameters α, β, and γ will in the following section be used to interpret the experimentally measured lattice constants.

## 4. Experimental results and discussion

Fig. 2 shows representative sections of XRD $\theta$-$2\theta$ patterns, from $WN_x$ layers deposited on $Al_2O_3(0001)$ at $T_s = 500$, 600, 700, and 800 °C. For clarity purposes, the plotted intensities have been reduced by a factor of 50 for $41° < 2\theta < 42.5°$ near the intense substrate reflection for all patterns, and by a factor of 100 for the $T_s = 800$ °C pattern for $38° < 2\theta < 41°$ near the intense BCC W 110 reflection. All layers exhibit a double peak feature at $2\theta = 41.685°$ and 41.793° due to reflections of the Cu $K_{\alpha 1}$ and $K_{\alpha 2}$ lines at the substrate $Al_2O_3$ 0006. The pattern from the layer deposited at $T_s = 500$ °C exhibits a peak with 19 ± 1 cps at $2\theta = 35.96 \pm 0.20°$, which is attributed to the 111 reflection for cubic β-WN. The angle is smaller than the reported value of $2\theta = 37.69°$ (JCPDF 01-075-1012), indicating a larger lattice constant for our layers which is attributed to the high N-content as discussed below. In addition, this pattern shows a 7.6 times weaker peak at $2\theta = 64.0 \pm 0.3°$ which is attributed to β-WN 220. No β-WN 002 peak is seen near the expected $2\theta = 43.8°$, indicating a negligible concentration of 001 oriented grains which may be due to epitaxial effects during grain nucleation on $Al_2O_3(0001)$.

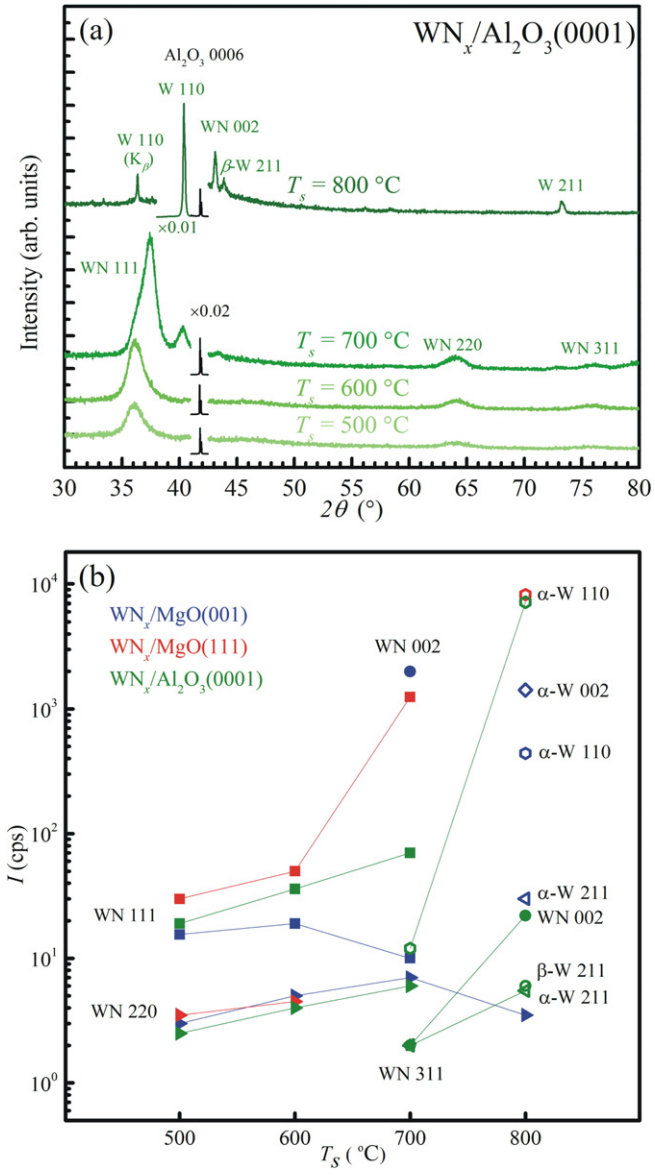


**Fig. 2.** (a) X-ray diffraction (XRD) patterns for $WN_x/Al_2O_3(0001)$ layers deposited at $T_s$ = 500, 600, 700, and 800 °C, and (b) summary plot from $WN_x$ deposited on MgO(001), MgO(111), and $Al_2O_3(0001)$, showing measured XRD peak intensities from β-WN 111, 220, 002, and 311, from α-W 110, 002, and 211, and from β-W 211 reflections, vs $T_s$ = 500–800 °C.

The layer has a strong 111-preferred orientation, since a random grain orientation is expected to lead to a β-WN 220 peak which is just 2.8 times smaller than the β-WN 111 peak [JCPDF 01-075-1012]. The pattern from the $T_s = 600$ °C layer indicates a similar 111 preferred orientation, with the β-WN 111 peak at $2\theta = 36.06 \pm 0.13°$ being 9.0 times stronger than the 220 peak. The 111 peak intensity is 36 ± 1 cps, which is 1.9 times larger than for $T_s = 500$ °C, indicating that the higher substrate temperature facilitates better long-range ordering, leading to a higher crystalline quality. However, the full-width at half-maximum remains relatively large, 1.7° and 1.5° for $T_s = 500$ and 600 °C, indicating considerable strain variations and/or point defects which limit the X-ray coherence length along the growth direction in these samples. For comparison, these widths are ~5 times larger than the corresponding width from an epitaxial β-WN(111)/MgO(111) layer, which is included in the summary analyses below and has already been discussed in detail in Ref. [35]. Increasing $T_s$ to 700 °C results in a $WN/Al_2O_3(0001)$ layer with an XRD pattern, shown in Fig. 2(a), which is still dominated by a relatively broad β-WN 111 peak with an intensity of 70 ± 2 cps. However, in contrast to $T_s \leq 600$ °C, the peak is shifted by 1.3° to the right, indicating a decreasing lattice constant which is attributed to an increasing N-vacancy concentration, as discussed below. The peak is asymmetric, with a shoulder to the left of the peak maximum, indicating that some regions in this layer have a larger and varying lattice parameter (4.21–4.32 Å) than the bulk of the sample with 4.17 Å, consistent with Ref. [35]. In addition, the pattern shows weaker peaks with 2 ± 1, 6 ± 1, and 2 ± 1 cps due to β-WN 002, 220, and 311 reflections, respectively, as well as small W 110 and 211 peaks with 12 ± 1 and 2 ± 1 cps at $2\theta = 40.24°$ and 72.9 ± 0.2°, respectively. The presence of these latter two peaks indicates that this sample contains some grains with a BCC α-W phase, suggesting a reduction of the nitrogen content in this layer which is consistent with the compositional analyses presented below. This effect becomes much more pronounced at our highest deposition temperature of 800 °C. The pattern shows a dominant W 110 peak with 7150 ± 50 cps, while the W 211 peak at $2\theta = 73.1 \pm 0.1°$ with 5 ± 1 cps is weak, suggesting a strong W 110 preferred orientation for this layer. In contrast to the lower deposition temperatures, the pattern shows no β-WN 111 peak but a β-WN 002 peak with 22 ± 1 cps. The peak at $2\theta = 43.74°$ with 6 ± 1 cps is attributed to β-W (A-15 structure) [55] while the peak at $2\theta = 36.23°$ is a measurement artifact, due to the $K_\beta$ X-ray line. The dominance of the W reflections in this pattern suggests a reduced nitrogen concentration for layers deposited at $T_s$ = 800 °C, consistent with a previous study suggesting nitrogen loss from tungsten nitrides at elevated temperatures (>820 °C) [56]. The slightly lower value for the temperature for nitrogen loss in our study may be related to different temperature calibration in the two studies. The peak position of the W 110 reflection indicates a lattice constant of 3.167 Å for the BCC W phase. This is 0.06% larger than the reported pure W lattice constant of 3.165 Å, which indicates a slight lattice expansion that may be associated with interstitial nitrogen within the W lattice.

Similar X-ray diffraction analyses as those shown in Fig. 2(a) have also been done for layers grown on MgO(001) and MgO(111) substrates at $T_s$ = 500–800 °C (not shown). The results for growth on MgO(111) are similar to those presented above for $Al_2O_3(0001)$ substrates. In particular, the patterns for $T_s$ = 500, 600, and 700 °C are dominated by β-WN 111 peaks at $2\theta = 35.6 \pm 1.0°$, 36.2 ± 1.0°, and 37.359 ± 0.001°, respectively, while $T_s$ = 800 °C leads to an intense W 110 peak of $8.20 \pm 0.05 \times 10^3$ cps but no detectable WN peak. Growth on MgO(001) results in dominant β-WN 111 peaks for $T_s$ = 500–600 °C, but a strong β-WN 002 peak at $2\theta = 42.7 \pm 0.1°$ with 2.0 ±

$0.2 \times 10^3$ cps for $T_s = 700$ °C which is attributed to epitaxial growth as we have already previously reported in Ref. [35], while $T_s = 800$ °C again yields BCC W.

Fig. 2(b) summarizes the XRD results from all samples in this study including those presented in detail in Fig. 1(a). It is a plot of the detected peak intensities from the $WN_x$ layers grown on the three substrates MgO(001), MgO(111), and $Al_2O_3$(0001), as a function of deposition temperature $T_s = 500$–800 °C. At $T_s = 500$ °C, the dominant peak for all three substrates is due to the β-WN 111 reflection. In particular, the 111 peak intensity from $WN_x$/MgO(111) is 30 cps, which is 8.6 times stronger than the 220 peak, while for $WN_x$/MgO(001), the 111 peak (15 cps) is 5.2 times stronger than the 220 peak, and the corresponding factor for $WN_x/Al_2O_3$(0001) is 7.6. These factors are considerably larger than the expected ratio of 111 vs 220 peak intensities for randomly oriented grains, with reported values of 2.8 for cubic WN [JCPDF 01-075-1012], 3.3 for cubic β-$W_2N$ [JCPDF 00-025-1257], and ranges from 1.6–3.3 for other cubic transition metal nitrides [JCPDF 01-074-8390, 00-025-1410, 01-074-1218, 00-049-1283, 00-038-1420, 00-035-0768, 00-031-1493, 01-075-1012, 00-025-1257]. Thus, all $WN_x$ layers grown at $T_s = 500$ °C show a clear 111 preferred orientation, consistent with reports from other cubic transition metal nitrides which exhibit 111 textures when deposited under kinetically limited conditions, that is, at low temperature and low ion-bombardment flux and/or energy, while 001 texture becomes preferred at higher temperatures and/or ion bombardment [57,58].

The $WN_x$ layers grown at an increased temperature of $T_s = 600$ °C also exhibit a 111 texture. Their β-WN 111 XRD peak intensity is 1.2, 1.7, and 1.9 times higher than for $T_s = 500$ °C for $WN_x$/MgO(001), $WN_x$/MgO(111), and $WN_x/Al_2O_3$(0001), respectively, as indicated by the lines that connect the plotted data points in Fig. 1(a) and are drawn to guide the eye. Similarly, the 220 intensities also increase with increasing $T_s$, indicating that the peak ratios remain approximately constant. This suggests that the crystalline quality and/or the grain orientation along the growth direction increase with $T_s$, while the relative fraction of 111 vs 220 oriented grains remains approximately constant as $T_s$ is increased from 500 and 600 °C. We note, though, that the 111 intensity for $WN_x$/MgO(001) deposited at $T_s = 600$ °C is only 3.8 times stronger than for the β-WN 220 peak, just slightly larger than the expected factor of 2.8 for randomly orientated β-WN, indicating a relatively weak 111 preferred orientation for this $WN_x$/MgO(001) layer in comparison to the 2.4–2.9-times stronger textured $WN_x$/MgO(111) and $WN_x/Al_2O_3$(0001) layers determined from comparison of the 111 and 220 peak intensities. We attribute the weak 111 texture on MgO(001) to an epitaxial bias that favors 001 oriented $WN_x$, while kinetic constraints still favor a 111 orientation.

Increasing $T_s$ to 700 °C results in considerable microstructural changes: Growth on MgO(111) yields an XRD pattern with a single intense β-WN 111 peak of 1250 cps at 37.36°, while no other $WN_x$ grain orientation or phase can be detected. The 111 peak is 25 times more intense than the corresponding peak for $T_s = 600$ °C, indicating strong 111-alignment for this layer and, in combination with previously reported XRD φ-scans and reciprocal space maps [35], demonstrates epitaxial growth of β-WN(111) on MgO(111). Similarly, $WN_x$ deposited on MgO(001) results in a dominant XRD peak. In this case it is a β-WN 002 peak of 2000 cps at 42.72°, while secondary β-WN 111 and 220 peaks are 2–3 orders of magnitude weaker with 10 and 7 cps, respectively. Consistent with our previous report in Ref. [35], this layer consists of an epitaxial β-$WN_x$(001)/MgO(001) matrix with a small concentration of misoriented β-WN grains. In contrast, deposition on $Al_2O_3$(0001) at $T_s = 700$ °C results in a 111-textured polycrystalline layer, as also shown in Fig. 2(a). That is, for $Al_2O_3$(0001) substrates, the trend from $T_s = 500$ and 600 °C is continued to $T_s = 700$ °C: The ratio between the different β-WN XRD peak intensities remains independent of $T_s$, while the crystalline quality and/or the grain orientation continues to improve, based on the 50–94% higher XRD peak intensities for $T_s = 700$ °C vs $T_s = 600$ °C. In addition, the XRD pattern from this layer also exhibits relatively weak 110 and 211 BCC W peaks with 12 and 2 cps, indicating that a small fraction of grains in this layer have lost the majority of their nitrogen.

For the highest growth temperature $T_s = 800$ °C, all XRD patterns are dominated by peaks associated with the α-W (BCC) phase. The pattern from the $WN_x$/MgO(001) layer exhibits strong α-W 002 and 110 peaks with 1420 and 440 cps, respectively, a weaker α-W 211 peak with 30 cps, and also a very weak β-WN 220 peak with 3.5 cps, indicating that only a small fraction of this layer forms a nitride phase. $WN_x$/MgO(111) shows a single intense α-W 110 peak of 8200 cps. Similarly, the pattern from the $WN_x/Al_2O_3$(0001) layers exhibits an intense α-W 110 peak of 7150 cps, but also a weak β-W 211 peak of 6 cps, a weak α-W 211 of 5.5 cps and a β-WN 002 peak of 22 cps. These results from $T_s = 800$ °C indicate nitrogen loss in $WN_x$ layers at elevated temperatures, as discussed more quantitatively in the following paragraph.

Fig. 3 is a plot of the nitrogen to tungsten ratio $x$, as measured by EDS using a light-element-sensitive setup as described in the Experimental procedure section. The $WN_x$ layers grown at $T_s = 500$ °C are overstoichiometric, with measured compositions of $WN_{1.20}$ deposited on MgO(001), $WN_{1.17}$ deposited on MgO(111), and $WN_{1.11}$ deposited on $Al_2O_3$(0001). The corresponding compositions for $T_s = 600$ °C are $x = 1.21$, 1.14, and 1.12, indicating negligible changes in the nitrogen content between 500 and 600 °C. In contrast, $x$ decreases to 0.92, 0.83, and 0.93 for $T_s = 700$ °C and drops to $x = 0.06$, 0.06, and 0.04, respectively. These results are confirmed by X-ray photoelectron spectroscopy (not shown), which yield compositions within ±3% from those obtained by EDS with, for example, $x = 0.92$, 0.81, and 0.90 for $WN_x$ grown at $T_s = 700$ °C on MgO(001), MgO(111), $Al_2O_3$(0001), respectively.

The data in Fig. 3 clearly shows a decrease in the N-content with increasing $T_s$, from overstoichiometric $WN_x$ for $T_s \leq 600$ °C, to understoichiometric $WN_x$ for $T_s = 700$ °C, to nearly N-free $WN_x$ for $T_s = 800$ °C. This trend is consistent with the XRD data, as patterns for $T_s \leq 700$ °C exhibit β-WN peaks while the dominant peaks for $T_s = 800$ °C are associated with the α-W phase. We propose that the residual 4–6% N in samples deposited at 800 °C is due to small amounts of nitrogen remaining in α-W grains for $WN_x$/MgO(111) or due to small β-WN grains for $WN_x$/MgO(001) or $WN_x/Al_2O_3$(0001), as described in the above XRD results. We note that the XRD analysis in Fig. 2 indicates that the $WN_x/Al_2O_3$(0001) layer with $T_s = 700$ °C also contains α-W. This, in turn, means that the $WN_x$ grains in this layer may have a larger N-content than the overall measured composition of $x = 0.93$. However, the detected α-W 110 XRD peak is approximately three orders of magnitudes weaker than the corresponding peak for the $WN_x/Al_2O_3$(0001)

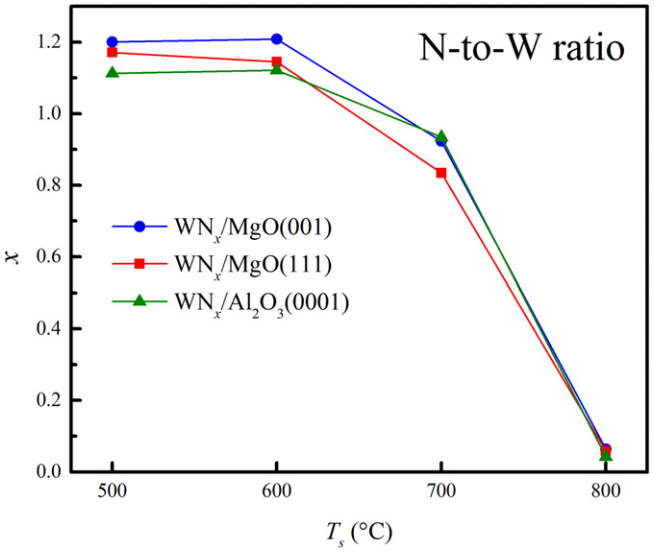


**Fig. 3.** Measured N/W ratio $x$ vs deposition temperature $T_s$ of $WN_x$ layers.

layer grown at $T_s = 800$ °C, suggesting that the α-W fraction in the $T_s = 700$ °C layer is very small, rendering this effect negligible. Therefore, for point defect concentration analyses below, we assume $x = 0.93$ is applicable for the $WN_x$ grains in the $WN_x/Al_2O_3(0001)$ layer with $T_s = 700$ °C. A decrease in the N-to-metal ratio with increasing $T_s$ has been reported for various other transition metal nitrides including $NbN_x$ above 900 °C [17], $CrN_x$ above 730 °C [59], $HfN_x$ above 650 °C [13], and $TaN_x$ above 400 °C [60], and has been attributed to a higher rate of nitrogen recombination and desorption at higher temperature, and the increasing importance of the entropy contribution to the free energy of the $N_2$ gas [17,61]. The measured N-content varies for different substrates, as presented in Fig. 3, this difference is relatively small (3–12%), but larger than the measurement uncertainty of ±3%. The reason for the differences is not known, but may be attributed to slight differences in the actual substrate temperature during deposition at nominally identical $T_s$, or also related to the changes in the nitrogen incorporation kinetics which is expected to be a function of the crystalline facet and therefore of the preferred layer orientation which is affected by the substrate.

Fig. 4(a) is a plot of the lattice constant for the cubic β-WN phase vs N-to-W ratio $x$. It is determined from the XRD peak positions of the strongest reflections in the θ-2θ patterns from each of the $WN_x$ layers grown on MgO(001), MgO(111), and $Al_2O_3(0001)$ at $T_s = 500$, 600, and 700 °C. The plot does not include data from the $T_s = 800$ °C samples, since they consist primarily of the BCC-W phase and possibly small inclusions of β-WN that cannot be detected or, for the case of $WN_x$/MgO(001), can be detected but have unknown composition since the N-content is not expected to match the measured average composition ($x = 0.06$) of the entire film which consists mostly of BCC-W. For all substrates, the lattice constant increases with increasing $x$, indicating that the lattice expands to incorporate the additional nitrogen, as also indicated by the dashed purple line which is a linear fit through all data points. More specifically, it increases for the $WN_x$/MgO(001) layers from 4.234 ± 0.009 Å for $x = 0.92$ grown at $T_s = 700$ °C to 4.322 ± 0.012 Å and 4.339 ± 0.023 Å for $x = 1.21$ and 1.20 with $T_s = 600$ °C and 500 °C. For $WN_x$/MgO(111), the lattice constant also increases with increasing $x$ from 4.169 ± 0.001 Å for $x = 0.83$ deposited at $T_s = 700$ °C to 4.301 ± 0.115 Å for $x = 1.14$ at 600 °C and 4.357 ± 0.118 Å for $x = 1.17$ at $T_s = 500$ °C. The two samples deposited on MgO(111) at the lower temperatures of $T_s = 500$–600 °C show larger error bars in the lattice constant due to the proximity of the 111 peak from the $WN_x$ layers to the intense MgO 111 substrate peaks. The lattice constant of $WN_x/Al_2O_3(0001)$ increases from 4.173 ± 0.070 Å for $x = 0.93$ deposited at $T_s = 700$ °C to 4.314 ± 0.015 Å for $x = 1.12$ at 600 °C and 4.325 ± 0.023 Å for $x = 1.11$ deposited at $T_s = 500$ °C. The large error bar in the lattice constant for the $WN_{0.93}/Al_2O_3(0001)$ sample deposited at 700 °C suggests strain or composition variations throughout the sample, causing a varying lattice constant [62], consistent with the observation presented in Fig. 2(a) and (b) that this sample contains small inclusions of BCC W grains which may be the result of spatial or temporal temperature variations, estimated to be ±25 °C, during growth of this sample. We also note that the plotted values are out-of-plane lattice constants which may, due to strain, slightly differ from the relaxed lattice constants. For example, a biaxial compressive stress would lead to an out-of-plane lattice constant that is greater than the corresponding relaxed lattice constant [11]. We have previously reported on our efforts to measure the strain in epitaxial $WN_x$ layers by XRD reciprocal space mapping, and have found in-plane strain values which are comparable to the experimental uncertainty, with values of $\varepsilon_{||} = 0.023 \pm 0.020$ (tensile) and $\varepsilon_{||} = -0.001 \pm 0.002$ (relaxed) for WN/MgO(111) and WN/MgO(001) grown at $T_s = 700$ °C, respectively [35].

We discuss the measured lattice constants for cubic $WN_x$ using the calculated values presented in Section 3 for stoichiometric and off-stoichiometric compositions. For this purpose, the fitting curves presented in Fig. 1(b) are reproduced in Fig. 4(a), illustrating the predicted lattice constants for β-$WN_x$ where the upper left and right curves correspond

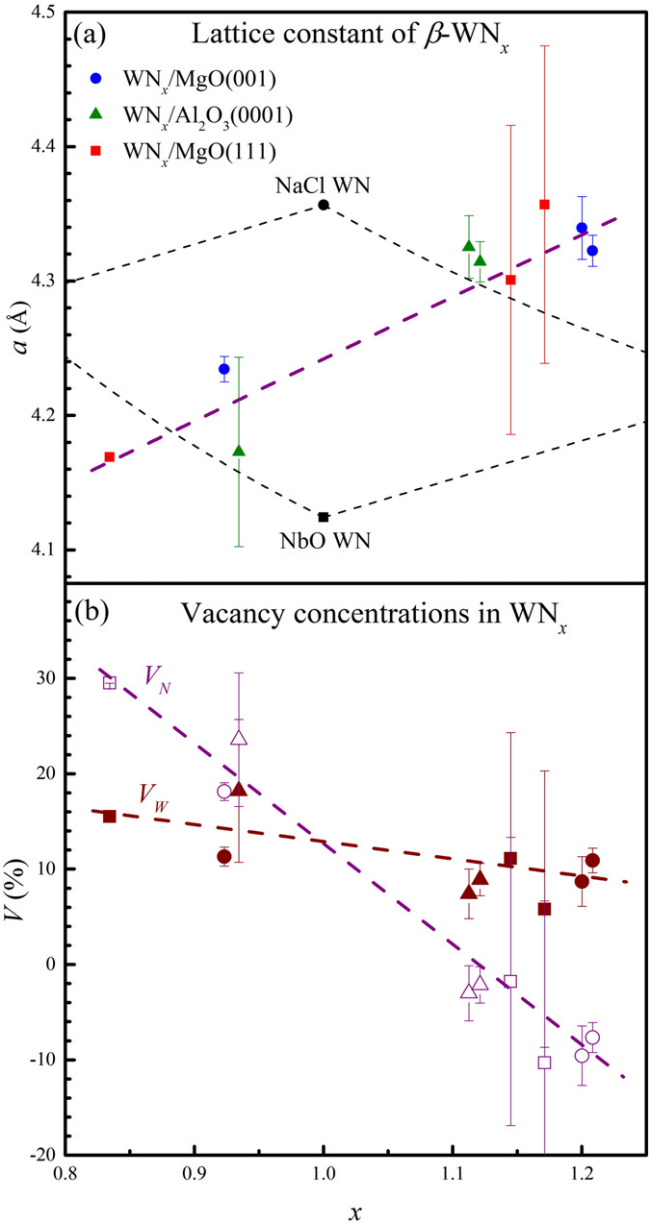


**Fig. 4.** (a) Measured out-of-plane lattice constants $a$ vs composition $x$ of $WN_x$ layers deposited on MgO(001), MgO(111), and $Al_2O_3(0001)$. The dashed purple line is a linear fit through all data points while the black symbols for stoichiometric WN in the rock-salt and NbO structures and the black dashed lines are computational results reproduced from Fig. 1(b). (b) Tungsten and nitrogen vacancy concentrations $V_W$ and $V_N$, as obtained from the measured lattice constants and Eq. (1). Circles, squares, and triangles represent data from $WN_x$/MgO(001), $WN_x$/MgO(111), and $WN_x/Al_2O_3(0001)$, respectively, while lines are from linear fitting. (For interpretation of the references to color in this figure legend, the reader is referred to the web version of this article.)

to a rock-salt structure containing N or W vacancies, respectively, and the lower left and right curves correspond to $WN_x$ in the NbO structure with some of the cation or anion vacant positions filled with W or N, respectively. The experimental data can be divided into two regions: (1) Layers deposited at $T_s = 500$–600 °C have lattice constants of 4.30–4.36 Å and compositions of $x = 1.11$–1.21. These data points are near the upper right simulation curve, suggesting that their structure can be described as a rock-salt phase that contains tungsten vacancies. (2) In contrast, growth at $T_s = 700$ °C yields $a = 4.17$–4.23 Å and $x = 0.83$–0.93. This group of data points approximately match the lower left curve, indicating that the structures may be best described by a NbO phase for which some vacant cation sites are filled with W. To illustrate this point further, Fig. 4(b) is a plot of the tungsten and nitrogen

vacancy concentrations $V_W$ and $V_N$ for the nine measured lattice constants presented in Fig. 4(a). The plotted values are determined using Eq. (1) including the numerical values for α, β, and γ that correspond to the lines in Figs. 1(b) and 4(a), and using the expression $x = (1 - V_N) / (1 - V_W)$ which relates the overall composition to the vacancy concentrations.

The tungsten vacancy concentration is 11–18% for the layers which are grown at 700 °C and are understoichiometric with $x = 0.83$–$0.93$. It decreases to $V_W = 6$–$11\%$ for the overstoichiometric layers with $x = 1.11$–$1.21$ and $T_s = 500$–$600$ °C. This decreasing trend with increasing $x$ is also indicated in Fig. 4(b) with a dashed line obtained from a linear fit. The trend is initially counter intuitive, since a decreasing $V_W$ corresponds to an increasing occupation of cation sites, while an increasing $x$ corresponds to an increasing anion to cation ratio. We attribute the negative slope of $V_W$ vs $x$ primarily to a temperature effect, while the change in $x$ is accounted for by nitrogen vacancies as discussed below. More specifically, an increase in growth temperature leads to a larger tungsten vacancy concentration. This is fully consistent with our first-principles calculations showing that the NbO structure is more stable than the rock-salt structure. Thus, our predicted lowest energy configurations exhibit $V_W = 25\%$. Correspondingly, increasing $T_s$ is expected to lead to structures which are closer to thermodynamic equilibrium, which corresponds to an increase in $V_W$ towards the predicted maximum of 25%, exactly as observed experimentally. The nitrogen vacancy concentration shows a much stronger composition dependence, decreasing from $V_N = 18$–$29\%$ for $x = 0.83$–$0.93$ to a negative $V_N = -2\%$ to $-10\%$ for $x = 1.11$–$1.21$. The negative values are a direct consequence of data points in Fig. 4(a) laying above the curve for the rock-salt structure containing W vacancies, which may be attributed to compressive strains, nitrogen interstitials, occupation of cation sites by N, or the formation of N-bubbles within the layer which form due to implantation of backscattered neutrals, as has previously been reported for other transition metal nitrides [63], and would correspond to a smaller-than-measured N-concentration within the $WN_x$ matrix. However, independent of the exact origin for the (unphysical) slightly negative $V_N$ values, the overall trend of a steeply decreasing $V_N$ with increasing $x$ is evident, as also indicated by the dashed line through the data. This trend shows that the decreasing anion-to-cation ratio with increasing $T_s$ is primarily accounted for by nitrogen vacancies. In summary, both W and N vacancy concentrations decrease with increasing $x$ in $WN_x$ layers. This trend is primarily attributed to growth temperature effects, where a larger $T_s$ helps to overcome kinetic barriers to move the system closer to the equilibrium structure, that is (1) towards the thermodynamically favorable cubic NbO structure which corresponds to the rock-salt structure with 25% of both W and N vacancies, and (2) to a lower N content within the nitride due to the high entropy of the competing $N_2$ vapor phase.

Fig. 5 shows measured physical properties including electrical resistivity $\rho$, elastic modulus $E$ and hardness $H$ of $WN_x$/MgO(001), $WN_x$/MgO(111), and $WN_x/Al_2O_3$(0001) layers as a function of $T_s = 500$–$800$ °C. The measured resistivity plotted in Fig. 5(a) decreases continuously with increasing growth temperature for all three sample sets. For $T_s = 500$ °C, $\rho = 4.5 \pm 0.2 \times 10^3$, $4.4 \pm 0.2 \times 10^3$, and $4.5 \pm 0.2 \times 10^3$ μΩ-cm for layers grown on MgO(001), MgO(111), and $Al_2O_3$(0001), respectively. The values decrease to $2.7 \pm 0.1 \times 10^3$, $2.6 \pm 0.1 \times 10^3$, and $3.2 \pm 0.1 \times 10^3$ μΩ-cm for $T_s = 600$ °C and to $1.6 \pm 0.1 \times 10^3$, $1.9 \pm 0.1 \times 10^3$, and $1.1 \pm 0.2 \times 10^3$ μΩ-cm for $T_s = 700$ °C. That is, the $WN_x$ layers in this study exhibit a range of resistivities from $1.1$–$4.5 \times 10^{-5}$ Ω-m, which is within the range of previously reported values for $WN_x$ of $0.1$–$5.0 \times 10^{-5}$ Ω-m [26,37,41,64–66], while other reports on $WN_x$ layers including samples obtained by MOCVD or sputtering at high working gas pressures or high ion bombardment energies indicate even higher resistivities ranging from $10^{-4}$–$10^{-1}$ Ω-m [33,38,39,44,67,68], which is likely due to their lower crystalline quality. The layers grown at $T_s = 800$ °C, which, as discussed above, consist primarily of BCC-W grains and have a low nitrogen concentration corresponding to $x = 0.06$, 0.06, and 0.04, respectively, have resistivities of $50 \pm 2$, $42 \pm 1$, and $48 \pm 2$ μΩ-cm. These values are higher than the reported 5.3 μΩ-cm for pure bulk W [69], likely due to the nonzero nitrogen content in these films. However, W films that were sputter deposited in Ne gas at room temperature have been reported to exhibit a considerably higher resistivity of 132 μΩ-cm [67].

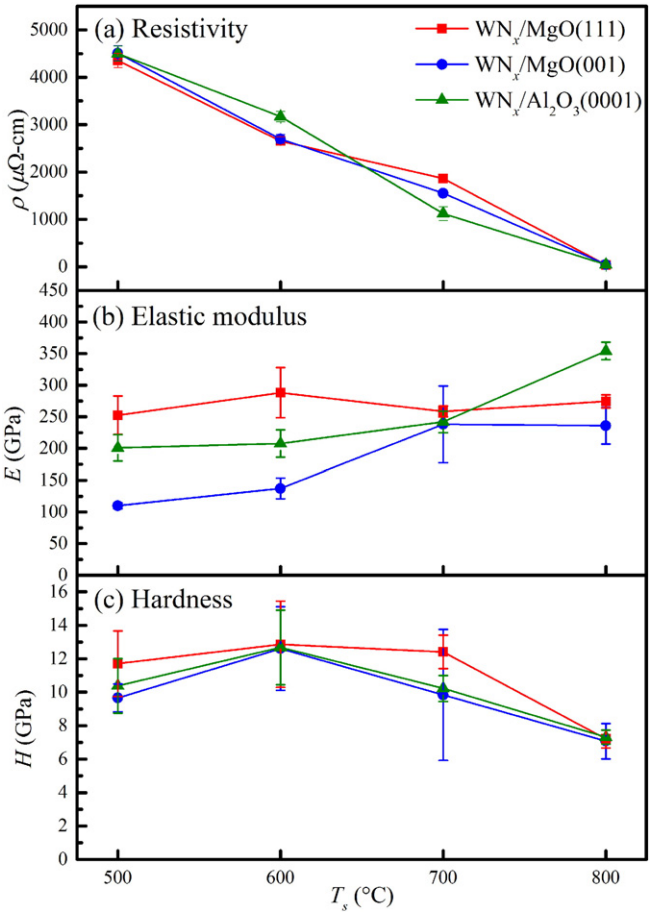


**Fig. 5.** (a) Resistivity $\rho$, (b) Young's modulus $E$, and (c) hardness $H$, vs deposition temperature $T_s$ of $WN_x$ samples deposited on MgO(001), MgO(111), and $Al_2O_3$(0001).

We attribute the decrease in resistivity with increasing $T_s$ primarily to an increased crystalline quality and grain size at higher deposition temperatures, reducing the weak carrier localization which has been used to describe electron transport in various transition metal nitrides including CrN(001) [70,71], $HfN_x$(001) [13], $TaN_x$(001) [18], $Sc_{1-x}Ti_xN$(001) [72], $Ti_{1-x}W_xN$(001) [73], $Sc_{1-x}Al_xN$(001) [74], NbN [17], and $NbC_xN_{1-x}$(001) [61]. In addition, the larger N vacancy concentration at higher $T_s$ may also contribute to the reduced resistivity, as nitrogen vacancies introduce additional electron carriers, raising the Fermi level further into the W 5*d* bands, which leads to more metallic conduction and may more than compensate for the expected additional electron scattering [11] at the localized states of N vacancies. In addition, we note the minor differences in resistivities measured for samples grown at the same temperature but on different substrates, which we attribute to microstructural differences including grain size, orientation, and grain boundary structure. In particular, the substrate affects the nucleation kinetics and therefore the nuclei size which, in turn, determines the column width, but also the preferred orientation which affects grain boundaries and the length scales for surface diffusion, resulting in variations in grain size and grain boundary electron reflection coefficients.

The elastic modulus of the $WN_x$ layers is plotted in Fig. 5(b), showing the trends in the elastic moduli versus growth temperature for the three

different substrates. $WN_x$/MgO(111) layers exhibit an elastic modulus which is nearly independent of $T_s$ = 500–700 °C, varying only from 253 ± 30 to 288 ± 40 to 259 ± 9 GPa despite the variation in microstructure and nitrogen content. Layers on $Al_2O_3$(0001) show similar overall moduli as on MgO(111), but suggest a slight increase from $E$ = 201 ± 21 to 208 ± 22 to 242 ± 17 GPa for $T_s$ = 500, 600, and 700 °C, respectively. In contrast, the $WN_x$/MgO(001) layers have considerably lower moduli and show a clear increase with increasing growth temperature, from 110 ± 5 GPa to 137 ± 16 GPa to 238 ± 61 GPa for $T_s$ = 500, 600, and 700 °C, respectively. The elastic moduli for the nitrogen rich samples deposited at $T_s$ = 500–600 °C exhibit a distinct dependence on the substrate. In particular, $E$ is largest for $WN_x$/MgO(111), smaller for $WN_x$/$Al_2O_3$(0001), and smallest for $WN_x$/MgO(001). This is exactly the same trend as observed in Fig. 2(b) for the 111-texture, with the strongest 111 preferred orientation for $WN_x$/MgO(111), a weaker texture for $WN_x$/$Al_2O_3$(0001) and only a slight 111 preferred orientation for $WN_x$/MgO(001). Therefore, we attribute the particularly low elastic moduli for $WN_x$/MgO(001) deposited at 500 and 600 °C to the weak 111 texture. In addition, these two samples have the highest measured N content with $x$ = 1.20 and 1.21, which may cause a low adatom mobility during deposition [75] due to a high N surface coverage, and therefore may result in underdense grain boundaries and an overall underdense microstructure which is expected to be the cause for the reduced elastic modulus. In contrast, $T_s$ = 700 °C yields $E$ values that are nearly independent of the substrate, suggesting that the higher crystalline quality of these layers in combination with the lower N content define the modulus more consistently. This is so despite that the different substrates result in different crystalline orientations of the $WN_x$, suggesting that the elastic anisotropy of β-WN is small/negligible, which is, however, in contradiction with our previous work suggesting an elastic anisotropy ratio of $A$ = 1.6 [35]. The layers deposited at $T_s$ = 800 °C have measured elastic moduli of 236 ± 29, 274 ± 10, and 354 ± 14 GPa. These layers contain only 4–6% N, they consist primarily of the BCC W phase, and their elastic modulus is in between 410 and 209 GPa, the known bulk value for pure W and the reported modulus for a 0.25 μm thick W layer on Si [76].

The measured elastic moduli from our β-WN layers can be compared to previous studies in which nanoindentation has been used to determine mechanical properties of $WN_x$ layers [28,32–34,38,40,43]. Reported values for the $WN_x$ elastic modulus range from $E$ = 240–430 GPa [32,34,40], with an increase in the N-to-W ratio from $x$ = 0.61–0.71 leading to a decrease in $E$ from 305 to 275 GPa [40], or for $x$ = 0.43, 0.89, and 1.38 to $E$ = 380, 380, and 325 GPa [32], with the latter value being further reduced through strain relaxation upon annealing to $E$ = 285 GPa [32]. This suggests that an increase in nitrogen content results in a decrease in the elastic modulus, consistent with the relatively low $E$ values of our samples with large N contents of $x$ ≥ 1.20. We note here that smaller N-to-W ratios also yield a reduced modulus $E_r$ = 279–224 GPa for samples with $x$ = 0.17–0.5 deposited by PLD and $E_r$ = 313–284 GPa for sputtered $WN_x$ with $x$ = 0.11–0.25 [34], while phase and intrinsic stress also affect $E$, for example, hexagonal $WN_{1.17}$ with a compressive stress of − 12.6 GPa exhibits a high $E$ = 430 GPa [40].

The hardness of the $WN_x$ samples is presented in Fig. 5(c) as a function of $T_s$ for the three substrate types. It is relatively independent on both the growth temperature and the substrate. The hardness of $WN_x$/MgO(001) varies from $H$ = 9.7 ± 0.8 to 12.6 ± 2.5, 9.8 ± 3.9, and 7.1 ± 1.1 GPa at $T_s$ = 500 °C, 600 °C, 700 °C, and 800 °C respectively. $WN_x$/MgO(111) increases in hardness from $H$ = 11.7 ± 2.0 GPa at 500 °C to 12.9 ± 2.6 GPa at 600 °C before decreasing to 12.4 ± 1.0 GPa at 700 °C and further to 7.2 ± 0.5 at 800 °C. $WN_x$/$Al_2O_3$(0001) layers show a similar behavior, with $H$ varying from 10.4 ± 1.6 to 12.7 ± 2.2, 10.2 ± 0.8, and 7.3 ± 0.4 GPa. The hardness values for the nearly N-free samples deposited at $T_s$ = 800 °C, 7.1 ± 1.1, 7.2 ± 0.5, and 7.3 ± 0.4 GPa, are between the reported bulk value for W of 6.6 ± 0.2 GPa and the reported 8 GPa for 1-μm-thick W deposited on MgO [76].

The hardness of $WN_x$ has previously been reported to range from 5 to 39 GPa [28,33,34,38,40,43]. This large range is attributed to variations in microstructure, nitrogen content, layer density, and phase content. For example, the reported $H$ decreases from 32 to 26 GPa as $x$ increases in cubic $WN_x$ from 0.35 to 0.7, but $H$ increases again with increasing $x$ > 0.75 due to the formation of hexagonal phase inclusions [40]. In addition, $H$ is reported to increase with deposition power and nitrogen partial pressure but decrease with total gas pressure, providing a large range from 6 to 30 GPa in a single study [33]. Our hardness values fall within the lower half of the previously reported range, which we attribute to the β-WN phase despite the high $x$ = 0.83–1.21 and a relatively low ion-implantation defect density associated with the absence of an intentional substrate bias as well as with the relatively high deposition temperatures. We also note that the measured ratio $H/E$ is relatively low, ranging from 0.04 to 0.09. This suggests that our $WN_x$ layers are relatively brittle, which may be attributed to the presence of both cation and anion vacancies, causing an increased bonding directionality as the structure transitions from the rocksalt to the NbO phase, resulting in an increased shear modulus and, in turn, a more brittle mechanical response.

## 5. Conclusions

Polycrystalline and epitaxial $WN_x$ layers were deposited on MgO(001), MgO(111), and $Al_2O_3$(0001) substrates as a function of temperature $T_s$ = 500–800 °C. At low $T_s$ = 500–600 °C, the deposited $WN_x$ layers are polycrystalline, exhibit a slight 111 preferred orientation, and show an increasing crystalline quality with increasing temperature. $T_s$ = 700 °C results in the highest quality crystals, which are epitaxial β-WN(111) on MgO(111), epitaxial β-WN(001) on MgO(001) with small inclusions of misoriented grains, and highly 111-textured β-WN on $Al_2O_3$(0001) with a small inclusions of misoriented WN grains and of BCC W. Out-of-plane lattice constants decrease from 4.357–4.169 Å as $T_s$ increases from 500 to 700 °C, while $x$ decreases from 1.21 to 0.83 over the same temperature range. The resistivity decreases from $4.5 \times 10^3$ to 42 μΩ-cm with increasing $T_s$, which is primarily attributed to an increasing crystalline quality and grain size which reduces the carrier localization. The measured $WN_x$ hardness is nearly independent of the substrate. It increases slightly from 500 to 600 °C as the crystal quality increases, decreases slightly from 600 to 700 °C as the nitrogen content decreases, and decreases some more to 7.1 GPa for layers deposited at 800 °C which consist of mostly BCC W. Elastic moduli measured by nanoindentation show a wide variation between the three substrates at 500–600 °C due to the different degree of 111 preferred orientation which causes changes in the nitrogen surface coverage, adatom mobility and, in turn, layer density. $T_s$ = 700 °C results in more consistent values with $E$ = 238–259 GPa, which may be attributed to the higher crystalline quality and/or lower N content of these layers. Density functional calculations indicate that cubic $WN_x$ is considerably more stable in the NbO than the rock-salt structure. The predicted lattice constants as a function of $x$ for both, the vacancy-containing rock-salt structure and the NbO structure where some of the vacant sites are filled, are used to interpret the experimentally measured lattice constants and to quantitatively determine the W and N vacancy concentrations. $V_W$ increases slightly and $V_N$ increases strongly with increasing $T_s$ and a simultaneously decreasing $x$. The latter is attributed to N-loss at elevated temperatures associated with the large entropy of $N_2$ gas, while the increase in the density of both vacancy types suggests that the increased atomic mobility during deposition leads to a structure approaching the thermodynamically favored NbO structure.

## Acknowledgements

The authors acknowledge support by the National Science Foundation under Grant Nos. 1309490, 1234777, 1234872, 1537984, and

1629230. Computational resources were provided by the Center for Computational Innovations at RPI.

## References


[1] H. Holleck, Material selection for hard coatings, J. Vac. Sci. Technol. A 4 (1986) 2661.
[2] J.-E. Sundgren, A review of the present state of art in hard coatings grown from the vapor phase, J. Vac. Sci. Technol. A 4 (1986) 2259.
[3] J. Musil, Hard and superhard nanocomposite coatings, Surf. Coat. Technol. 125 (2000) 322–330.
[4] M. Georgson, The influence of preparation conditions on the optical properties of titanium nitride based solar control films, J. Vac. Sci. Technol. A 9 (1991) 2191.
[5] S. Niyomsoan, W. Grant, D. Olson, B. Mishra, Variation of color in titanium and zirconium nitride decorative thin films, Thin Solid Films 415 (2002) 187–194.
[6] M. Marlo, V. Milman, Density-functional study of bulk and surface properties of titanium nitride using different exchange-correlation functionals, Phys. Rev. B 62 (2000) 2899–2907.
[7] J.O. Kim, J.D. Achenbach, P.B. Mirkarimi, M. Shinn, S.A. Barnett, Elastic constants of single-crystal transition-metal nitride films measured by line-focus acoustic microscopy, J. Appl. Phys. 72 (1992) 1805–1811.
[8] A.B. Mei, R.B. Wilson, D. Li, D.G. Cahill, A. Rockett, J. Birch, L. Hultman, J.E. Greene, I. Petrov, Elastic constants, Poisson ratios, and the elastic anisotropy of VN(001), (011), and (111) epitaxial layers grown by reactive magnetron sputter deposition, J. Appl. Phys. 115 (2014) 214908.
[9] Z.T.Y. Liu, X. Zhou, S.V. Khare, D. Gall, Structural, mechanical and electronic properties of 3d transition metal nitrides in cubic zincblende, rocksalt and cesium chloride structures: a first-principles investigation, J. Phys. Condens. Matter 26 (2014) 025404.
[10] Z.T.Y. Liu, D. Gall, S.V. Khare, Electronic and bonding analysis of hardness in pyrite-type transition-metal pernitrides, Phys. Rev. B 90 (2014) 134102.
[11] C.-S. Shin, S. Rudenja, D. Gall, N. Hellgren, T.-Y. Lee, I. Petrov, J.E. Greene, Growth, surface morphology, and electrical resistivity of fully strained substoichiometric epitaxial $TiN_x$ ($0.67 \le x < 1.0$) layers on MgO(001), J. Appl. Phys. 95 (2004) 356.
[12] C.-S. Shin, D. Gall, N. Hellgren, J. Patscheider, I. Petrov, J.E. Greene, Vacancy hardening in single-crystal $TiN_x$(001) layers, J. Appl. Phys. 93 (2003) 6025.
[13] H.-S. Seo, T.-Y. Lee, I. Petrov, J.E. Greene, D. Gall, Epitaxial and polycrystalline $HfN_x$ ($0.8 \le x \le 1.5$) layers on MgO(001): film growth and physical properties, J. Appl. Phys. 97 (2005) 083521.
[14] T.-Y. Lee, D. Gall, C.-S. Shin, N. Hellgren, I. Petrov, J.E. Greene, Growth and physical properties of epitaxial CeN layers on MgO(001), J. Appl. Phys. 94 (2003) 921.
[15] E.O. Ristolainen, J.M. Molarius, A.S. Korhonen, V.K. Lindroos, A study of nitrogen-rich titanium and zirconium nitride films, J. Vac. Sci. Technol. A 5 (1987) 2184.
[16] C. Shin, Y. Kim, D. Gall, J.E. Greene, I. Petrov, Phase composition and microstructure of polycrystalline and epitaxial $TaN_x$ layers grown on oxidized Si(001) and MgO(001) by reactive magnetron sputter deposition, Thin Solid Films 402 (2002) 172–182.
[17] K. Zhang, K. Balasubramanian, B.D. Ozsdolay, C.P. Mulligan, S.V. Khare, W.T. Zheng, D. Gall, Growth and mechanical properties of epitaxial NbN(001) films on MgO(001), Surf. Coat. Technol. 288 (2016) 105.
[18] C.-S. Shin, D. Gall, Y.-W. Kim, P. Desjardins, I. Petrov, J.E. Greene, M. Odén, L. Hultman, Epitaxial NaCl structure δ-$TaN_x$(001): electronic transport properties, elastic modulus, and hardness versus N/Ta ratio, J. Appl. Phys. 90 (2001) 2879.
[19] L.E. Toth, Transition Metal Carbides and Nitrides, Academic Press, Inc., New York, New York, 1971.
[20] N. Schonberg, Contributions to the knowledge of the molybdenum–nitrogen and the tungsten–nitrogen systems, Acta Chem. Scand. 8 (1954) 204–207.
[21] H. Wang, Q. Li, Y. Li, Y. Xu, T. Cui, A.R. Oganov, Y. Ma, Ultra-incompressible Phases of Tungsten Dinitride Predicted From First Principles, 2009 1–4.
[22] S. Wang, X. Yu, Z. Lin, R. Zhang, D. He, J. Qin, J. Zhu, J. Han, L. Wang, H.K. Mao, J. Zhang, J. Zhao, Synthesis, crystal structure, and elastic properties of novel tungsten nitrides, Chem. Mater. 24 (2012) 3023–3028.
[23] Z.T.Y. Liu, X. Zhou, D. Gall, S.V. Khare, First-principles investigation of the structural, mechanical and electronic properties of the NbO-structured 3d, 4d and 5d transition metal nitrides, Comput. Mater. Sci. 84 (2014) 365–373.
[24] X. Zhou, D. Gall, S.V. Khare, Mechanical properties and electronic structure of anti-$ReO_3$ structured cubic nitrides, $M_3N$, of d block transition metals M: an ab initio study, J. Alloys Compd. 595 (2014) 80–86.
[25] M.J. Mehl, D. Finkenstadt, C. Dane, G.L.W. Hart, S. Curtarolo, Finding the stable structures of $N_{1-x}W_x$ with an ab initio high-throughput approach, Phys. Rev. B 91 (2015) 184110.
[26] M.L. Addonizio, A. Castaldo, A. Antonaia, E. Gambale, L. Iemmo, Influence of process parameters on properties of reactively sputtered tungsten nitride thin films, J. Vac. Sci. Technol. A 30 (2012) 031506.
[27] Y.G. Shen, Y.W. Mai, Microstructure and structure characteristics of cubic $WN_x$ compounds, Mater. Sci. Eng. A 288 (2000) 47–53.
[28] M. Wen, Q.N. Meng, W.X. Yu, W.T. Zheng, S.X. Mao, M.J. Hua, Growth, stress and hardness of reactively sputtered tungsten nitride thin films, Surf. Coat. Technol. 205 (2010) 1953–1961.
[29] O.J. Bchir, S.W. Johnston, A.C. Cuadra, T.J. Anderson, C.G. Ortiz, B.C. Brooks, D.H. Powell, L. McElwee-White, MOCVD of tungsten nitride ($WN_x$) thin films from the imido complex $Cl_4(CH_3CN)W(N^tPr)$, J. Cryst. Growth 249 (2003) 262–274.
[30] C.C. Baker, S.I. Shah, Reactive sputter deposition of tungsten nitride thin films, J. Vac. Sci. Technol. A 20 (2002) 1699.
[31] R.W.G. Wyckoff, Crystal Structures, Vol. I, 2nWiley, New York, 1963.
[32] T. Polcar, A. Cavaleiro, Structure, mechanical properties and tribology of W–N and W–O coatings, Int. J. Refract. Met. Hard Mater. 28 (2010) 15–22.
[33] K.K. Shih, D.B. Dove, Properties of W–N and Mo–N films prepared by reactive sputtering, J. Vac. Sci. Technol. A 8 (1990) 1359.
[34] E.C. Samano, A. Clemente, J.A. Díaz, G. Soto, Mechanical properties optimization of tungsten nitride thin films grown by reactive sputtering and laser ablation, Vacuum 85 (2010) 69–77.
[35] B.D. Ozsdolay, C.P. Mulligan, M. Guerette, L. Huang, D. Gall, Epitaxial growth and properties of cubic WN on MgO(001), MgO(111), and $Al_2O_3$(0001), Thin Solid Films 590 (2015) 276–283.
[36] Y.G. Shen, Y.W. Mai, D.R. McKenzie, Q.C. Zhang, W.D. McFall, W.E. McBride, Composition, residual stress, and structural properties of thin tungsten nitride films deposited by reactive magnetron sputtering, J. Appl. Phys. 88 (2000) 1380.
[37] L. Boukhris, J.-M. Poitevin, Electrical resistivity, structure and composition of d.c. sputtered $WN_x$ films, Thin Solid Films 310 (1997) 222–227.
[38] M. Bereznai, Z. Toth, A.P. Caricato, M. Fernandez, A. Luches, G. Majni, P. Mengucci, P.M. Nagy, A. Juhász, L. Nánai, Reactive pulsed laser deposition of thin molybdenum- and tungsten-nitride films, Thin Solid Films 473 (2005) 16–23.
[39] G. Soto, W. de la Cruz, F.F. Castillon, J.A. Diaz, R. Machorro, M.H. Farıas, Tungsten nitride films grown via pulsed laser deposition studied in situ by electron spectroscopies, Appl. Surf. Sci. 214 (2003) 58–67.
[40] P. Hones, N. Martin, M. Regula, L. Francis, Structural and mechanical properties of chromium nitride, molybdenum nitride , and tungsten nitride thin films, J. Phys. D. Appl. Phys. 36 (2003) 1023–1029.
[41] P.-C. Jiang, J.S. Chen, Y.K. Lin, Structural and electrical characteristics of W–N thin films prepared by reactive rf sputtering, J. Vac. Sci. Technol. A 21 (2003) 616.
[42] P. Boher, P. Houdy, P. Kaikati, L.J. Van Ijzendoorn, Radio frequency sputtering of tungsten/tungsten nitride multilayers on GaAs, J. Vac. Sci. Technol. A 8 (1990) 846.
[43] T. Yamamoto, M. Kawate, H. Hasegawa, T. Suzuki, Effects of nitrogen concentration on microstructures of $WN_x$ films synthesized by cathodic arc method, Surf. Coat. Technol. 193 (2005) 372–374.
[44] J.S. Becker, R.G. Gordon, Diffusion barrier properties of tungsten nitride films grown by atomic layer deposition from bis(tert-butylimido)bis(dimethylamido) tungsten and ammonia, Appl. Phys. Lett. 2239 (2003) 1–4.
[45] M. Nagai, K. Kishida, Thin film synthesis of tungsten nitride by the CVD method, Appl. Surf. Sci. 70 (71) (1993) 759–762.
[46] T. Nakajima, K. Watanabe, N. Watanabe, Preparation of tungsten nitride film by CVD method using $WF_6$, J. Electrochem. Soc. 134 (1987) 3175–3178.
[47] S. Vepřek, M. Haussmann, S. Reiprich, Superhard nanocrystalline $W_2N$/amorphous $Si_3N_4$ composite materials, J. Vac. Sci. Technol. A 14 (1996) 46.
[48] J.S. Chawla, D. Gall, Epitaxial Ag(001) grown on MgO(001) and TiN(001): twinning, surface morphology, and electron surface scattering, J. Appl. Phys. 111 (2012) 043708.
[49] G.M. Pharr, W.C. Oliver, Measurement of thin film mechanical properties using nanoindentation, MRS Bull. 17 (1992) 28–33.
[50] Y.-T. Cheng, C.-M. Cheng, Relationships between hardness, elastic modulus, and the work of indentation, Appl. Phys. Lett. 73 (1998) 614.
[51] F.M. Smits, Measurement of sheet resistivities with the four-point probe, Bell Syst. Tech. J. 37 (1958) 711–718.
[52] J.P. Perdew, K. Burke, M. Ernzerhof, Generalized gradient approximation made simple, Phys. Rev. Lett. 77 (1996) 3865–3868.
[53] G. Kresse, D. Joubert, From ultrasoft pseudopotentials to the projector augmented-wave method, Phys. Rev. B 59 (1999) 1758–1775.
[54] J.P. Perdew, A. Ruzsinszky, G.I. Csonka, O.A. Vydrov, G.E. Scuseria, L.A. Constantin, X. Zhou, K. Burke, Restoring the density-gradient expansion for exchange in solids and surfaces, Phys. Rev. Lett. 100 (2008) 136406.
[55] I.A. Weerasekera, S.I. Shah, D.V. Baxter, K.M. Unruh, Structure and stability of sputter deposited beta-tungsten thin films, Appl. Phys. Lett. 64 (1994) 3231.
[56] Y.G. Shen, Y.W. Mai, W.E. Mcbride, Q.C. Zhang, D.R. Mckenzie, Structural Properties and Nitrogen-loss Characteristics in Sputtered Tungsten Nitride Films, 2000 257–264.
[57] D. Gall, S. Kodambaka, M.A. Wall, I. Petrov, J.E. Greene, Pathways of atomistic processes on TiN(001) and (111) surfaces during film growth: an ab initio study, J. Appl. Phys. 93 (2003) 9086.
[58] L.E. Koutsokeras, G. Abadias, P. Patsalas, Texture and microstructure evolution in single-phase $Ti_xTa_{1-x}N$ alloys of rocksalt structure, J. Appl. Phys. 110 (2011) 043535.
[59] D. Gall, C.-S. Shin, T. Spila, M. Odén, M.J.H. Senna, J.E. Greene, I. Petrov, Growth of single-crystal CrN on MgO(001): effects of low-energy ion-irradiation on surface morphological evolution and physical properties, J. Appl. Phys. 91 (2002) 3589.
[60] C.-S. Shin, Y.-W. Kim, N. Hellgren, D. Gall, I. Petrov, J.E. Greene, Epitaxial growth of metastable δ-TaN layers on MgO(001) using low-energy, high-flux ion irradiation during ultrahigh vacuum reactive magnetron sputtering, J. Vac. Sci. Technol. A 20 (2002) 2007.
[61] K. Zhang, K. Balasubramanian, B.D. Ozsdolay, C.P. Mulligan, S.V. Khare, W.T. Zheng, D. Gall, Epitaxial $NbC_xN_{1-x}$(001) layers: growth, mechanical properties, and electrical resistivity, Surf. Coat. Technol. 277 (2015) 136.
[62] S.G. Malhotra, Z.U. Rek, S.M. Yalisove, J.C. Bilello, Strain gradients and normal stresses in textured Mo thin films, J. Vac. Sci. Technol. A 15 (1997) 345–352.
[63] D. Gall, I. Petrov, N. Hellgren, L. Hultman, J.E. Sundgren, J.E. Greene, Growth of poly- and single-crystal ScN on MgO(001): role of low-energy $N_2^+$ irradiation in determining texture, microstructure evolution, and mechanical properties, J. Appl. Phys. 84 (1998) 6034–6041.
[64] P. Jiang, Y. Lai, J.S. Chen, Dependence of crystal structure and work function of $WN_x$ films on the nitrogen content, Appl. Phys. Lett. 89 (2006) 122107.

[65] J. Lin, A. Tsukune, T. Suzuki, M. Yamada, Different effect of annealing temperature on resistivity for stoichiometric, W rich, and N rich tungsten nitride films, J. Vac. Sci. Technol. A 17 (1999) 936.
[66] S. Guruvenket, G.M. Rao, Bias induced structural changes in tungsten nitride films deposited by unbalanced magnetron sputtering, Mater. Sci. Eng. B 106 (2004) 172–176.
[67] K.J. Huber, C.R. Aita, Resistivity changes and phase evolution in W–N films sputter deposited in Ne–$N_2$ and Ar–$N_2$ discharges, J. Vac. Sci. Technol. A 6 (1988) 1717.
[68] T. Migita, R. Kamei, T. Tanaka, K. Kawabata, Effect of dc bias on the compositional ratio of $WN_x$ thin films prepared by rf-dc coupled magnetron sputtering, Appl. Surf. Sci. 170 (2001) 362–365.
[69] D. Choi, C.S. Kim, D. Naveh, S. Chung, A.P. Warren, N.T. Nuhfer, M.F. Toney, K.R. Coffey, K. Barmak, Electron mean free path of tungsten and the electrical resistivity of epitaxial (110) tungsten films, Phys. Rev. B 86 (2012) 045432.
[70] X.Y. Zhang, J.S. Chawla, R.P. Deng, D. Gall, Epitaxial suppression of the metal-insulator transition in CrN, Phys. Rev. B 84 (2011) 073101.
[71] X.Y. Zhang, J.S. Chawla, B.M. Howe, D. Gall, Variable-range hopping conduction in epitaxial CrN(001), Phys. Rev. B 83 (2011) 165205.
[72] D. Gall, I. Petrov, J.E. Greene, Epitaxial $Sc_{1-x}Ti_xN$(001): optical and electronic transport properties, J. Appl. Phys. 89 (2001) 401.
[73] F. Tian, J. D'Arcy-Gall, T.-Y. Lee, M. Sardela, D. Gall, I. Petrov, J.E. Greene, Epitaxial $Ti_{1-x}W_xN$ alloys grown on MgO(001) by ultrahigh vacuum reactive magnetron sputtering: Electronic properties and long-range cation ordering, J. Vac. Sci. Technol. A 21 (2003) 140.
[74] R.P. Deng, P.Y. Zheng, D. Gall, Optical and electron transport properties of rock-salt $Al_{1-x}Sc_xN$, J. Appl. Phys. (2015) (submitted).
[75] J.A. Thornton, The microstructure of sputter-deposited coatings, J. Vac. Sci. Technol. A 4 (1986) 3059.
[76] G. Abadias, S. Dub, R. Shmegera, Nanoindentation hardness and structure of ion beam sputtered TiN, W and TiN/W multilayer hard coatings, Surf. Coat. Technol. 200 (2006) 6538–6543.